ACS APPLIED NANO MATERIALS

www.acsanm.org Article

Au/SiO_2-Nanolaminated Plasmonic Nanoantennas as Refractive-Index-Insensitive and Transparent Surface-Enhanced Raman Spectroscopy Substrates

Wonil Nam, Junyeob Song, Seied Ali Safiabadi Tali, Henri J. Lezec, Amit Agrawal, and Wei Zhou*

Cite This: *ACS Appl. Nano Mater.* 2021, 4, 3175−3184 Read Online

ACCESS | Metrics & More | Article Recommendations | Supporting Information

ABSTRACT: Surface-enhanced Raman spectroscopy (SERS) has become a powerful technique for ultrasensitive biochemical detection providing molecular fingerprint information. Due to the strong dependence of surface plasmon resonance wavelength on plasmonic nanostructures' surrounding refractive index (RI), SERS enhancement factors (EFs) at hotspots are sensitive to changes in background RI, which is detrimental to quantitative SERS biochemical analysis in real-world applications with spatially and temporally varying RI matrices. This work reports on a tapered-shape nanolaminate plasmonic nanoantenna (TNLNA) platform that supports multiple, spatially overlapped, hybridized magnetoelectric localized surface plasmon modes revealing high SERS EFs (>10^7) and an insensitivity to background RI variations (between 1.30 and 1.60). Furthermore, we demonstrate that the uniform arrays of TNLNAs can be manufactured on flexible transparent polymer films to achieve backside-excitable and reversible SERS measurements for in situ label-free glucose monitoring on a skin phantom.

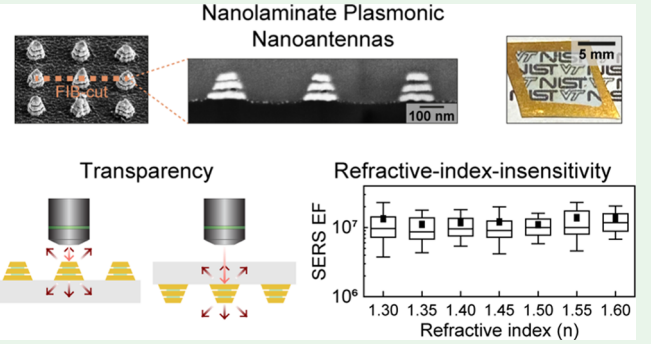

KEYWORDS: *multiresonant plasmonics, nanolaminate, surface-enhanced Raman spectroscopy (SERS), refractive-index-insensitive, in situ SERS*

1. INTRODUCTION

Surface-enhanced Raman spectroscopy (SERS) is an ultrasensitive, label-free, and noninvasive biochemical detection and analysis technique based on vibrational molecular fingerprint information.[1,2] Via excitation of localized surface plasmon (LSP) modes, plasmonic nanostructures can significantly enhance vibrational inelastic Raman scattering signals from analyte molecules at hotspots by orders of magnitude.[2] The LSP resonance wavelengths of plasmonic nanostructures strongly depend on their background refractive index (RI), allowing for RI-based optical sensing of interfacial analyte binding events.[3,4] Nevertheless, such high RI-sensitivity of plasmonic modes can significantly and negatively affect local SERS enhancement factors (EFs) to bias quantitative SERS analysis of diverse biological, clinical, environmental, and food samples with spatially or temporally varying RI matrices. For example, various intracellular and extracellular organelles in biological and clinical samples have different RI values between 1.30 and 1.60 with dynamically changing spatial distributions.[5,6] Therefore, quantitative SERS biochemical analysis faces a challenge because the RI-sensitive SERS response of even uniformly distributed hotspots can obscure a reliable relation between SERS signal intensities and actual analyte concentrations.[7] Moreover, a general approach for creating high-performance uniform SERS substrates is to densely pack plasmonic nanostructures with a single LSP resonance matching the excitation laser wavelength. Most studies developing high-performance SERS substrates focus on achieving high SERS EFs by increasing the hotspot density and improving the uniformity of hotspot distribution without considering the effects of RI background variations on the SERS performance.[1,2,7−11] Since typical SERS substrates only support a single LSP mode near the excitation laser wavelength, their SERS EFs show maximum values at the LSP resonance wavelength and are therefore sensitive to background RI variations.[12]

Our recent study reports that nanolaminate plasmonic crystals (NLPC) consisting of multilayered metal−insulator−metal (MIM) nanohole and nanoparticle arrays can serve as uniform high-performance SERS substrates with large SERS

Received: February 6, 2021
Accepted: March 1, 2021
Published: March 10, 2021

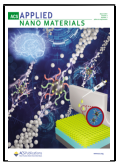

Scheme 1. Fabrication Procedure of TNLNAs[a]

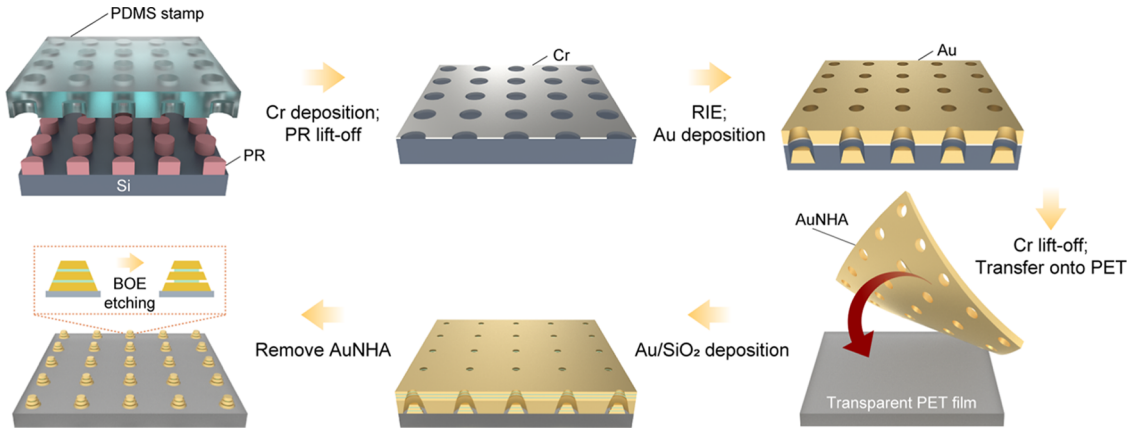

[a]PR; photoresists; RIE, reactive ion etching; and BOE, buffered oxide etchant.

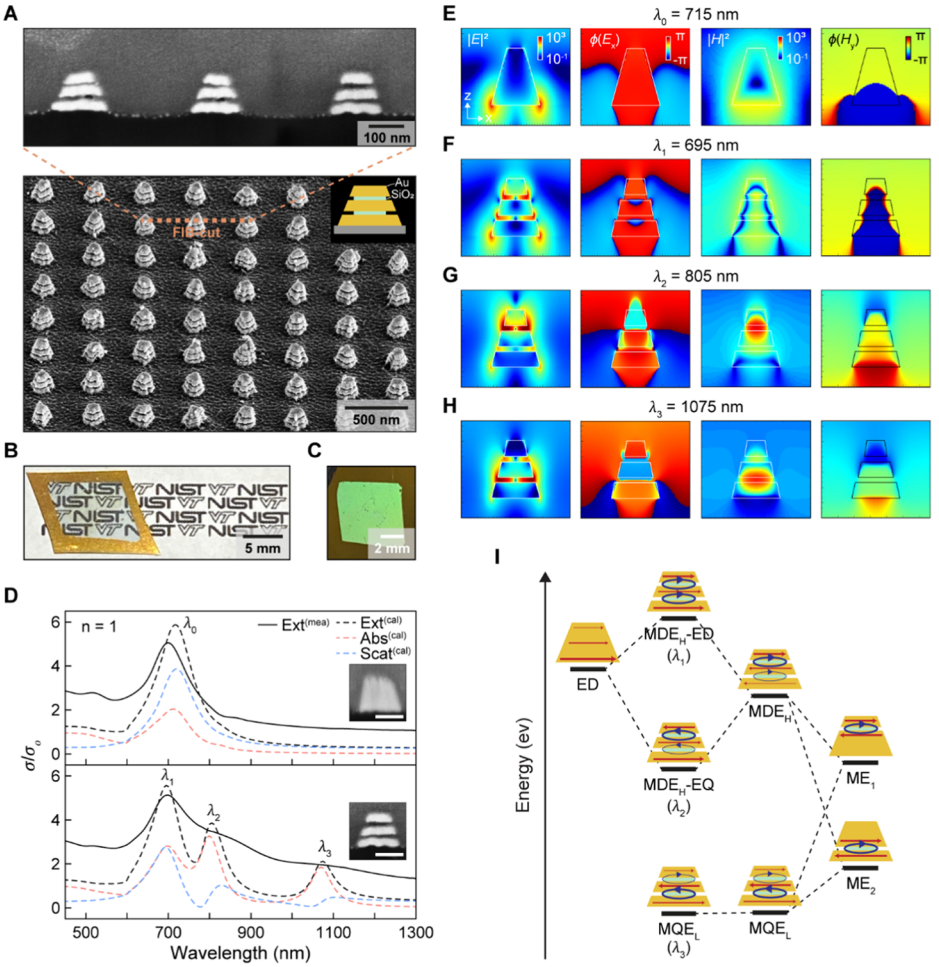

Figure 1. Optical properties and plasmon hybridization analysis of TNLNAs. (A) Cross-sectional (top) and top (bottom) view scanning electron microscope (SEM) images of TNLNAs. FIB, focused-ion-beam; (B, C) photograph images of TNLNAs. (D) Measurements (solid) and finite-difference time-domain (FDTD)-calculated (dashed) extinction spectra of TAuNPs (top) and TNLNAs (bottom) with absorption and scattering contributions, insets: cross-sectional SEM images of each structure. Scale bars: 100 nm. (E−H) FDTD-calculated distribution maps of $|E|^2$, $|H|^2$, $\phi(H_y)$, and $\phi(E_x)$ at resonant wavelengths of TAuNPs (λ_0 = 715 nm) and TNLNAs (λ_1 = 695 nm, λ_2 = 805 nm, and λ_3 = 1075 nm). (I) Energy diagram of plasmon hybridization processes in TNLNAs.

EFs (>10^7) insensitive to background RI variations between 1.30 and 1.60.[7]

By the hybridization between delocalized plasmonic modes in MIM nanohole arrays and localized plasmonic modes in MIM nanoparticles, NLPC can support multiple hybrid plasmonic modes over a broad spectral range to concentrate the excitation laser optical fields in hotspots at different background RI. However, due to the structural containment of

https://dx.doi.org/10.1021/acsanm.1c00389
ACS Appl. Nano Mater. 2021, 4, 3175−3184

interconnected MIM nanohole arrays, NLPC has low optical transparency and a large footprint. The opaque nature of NLPC SERS substrates prevents laser excitation and Raman signal collection from the backside, detrimental for applications such as wearable and implantable sensing, food safety, and environmental monitoring.[13,14] Furthermore, the large footprint of NLPC SERS substrates prevents their integration with other nanoscale devices (e.g., nanopillar electrodes) for multifunctional operations.[15,16]

Sandwichlike metal−insulator−metal (MIM) nanostructures support a high-energy antibonding electric dipole (ED) mode and a low-energy bonding magnetic dipole (MD) mode, which can serve as nanoscale plasmonic building blocks for constructing negative-index metamaterials and multiresonant composite nanoantennas.[17−19] Despite significant progress on the single-gap-based MIM plasmonic nanostructures,[20−22] there are only a few studies on vertically stacked (i.e., nanolaminate) MIM building blocks due to complex plasmon hybridization and difficulties in nanofabrication techniques.[23,24] Recent studies show that the nanolaminate plasmonic nanoantennas can support multiple hybrid LSP modes with spatial mode overlaps and provide independent spectral tuning capability for individual plasmon modes by simply controlling the out-of-plane geometries.[23,24] In spite of increasing research interest, what roles multiresonant nanolaminate plasmonic nanoantennas can play in the SERS applications have not been reported yet.

Here, we create tapered-shape nanolaminate plasmonic nanoantennas (TNLNAs) consisting of multilayered out-of-plane metal (Au) and insulator (SiO_2) nanodisks (Scheme 1 and Figure 1A) and investigate the effects of background RI changes on their multiresonant optical properties and SERS performance. We demonstrate that TNLNAs exhibit unique RI-insensitive SERS performance by supporting multiple hybridized magnetoelectric (ME) modes. Using soft nanolithography with a nanohole array deposition mask,[25−28] we fabricate dense periodic arrays of TNLNAs on a wafer-scale flexible transparent polymer film and demonstrate their capability to achieve in situ SERS detection of glucose molecules on a skin phantom. Furthermore, since TNLNAs exhibit broadband multiresonant optical properties with a nanoscale footprint, they can potentially integrate with other types of electrical and optical nanodevices to enable wavelength-multiplexed multifunctional operation at the nanoscale.

2. EXPERIMENTAL SECTION

2.1. TNLNA Fabrication. For the fabrication of TNLNAs on transparent flexible poly(ethylene terephthalate) (PET) films, we used a free-standing film of AuNHA as a physical deposition mask to create periodic arrays of multilayered MIM nanostructures (Scheme 1). To fabricate AuNHA, we first used a poly(dimethylsiloxane) (PDMS) photomask replicated from a silicon master patterned with nanopillar arrays.[25−28] The PDMS mask was in contact with a spin-coated positive-tone photoresist on a silicon wafer during the UV exposure process. Photoresist pillar arrays were developed, and a thin Cr layer (nominally 10 nm) was deposited using e-beam evaporation followed by sonication with acetone to lift-off the pillar arrays and create Cr nanohole arrays. Using reactive ion etching with O_2 and CF_4 mixtures (1:5), the silicon wafer was etched through the Cr nanohole arrays to create an undercut. Nominally 160 nm thick gold was deposited on the Cr nanohole arrays using e-beam evaporation to create AuNHA (Figure S1A,B). We then lifted-off AuNHA using Cr etchant and transferred it onto the PET film. A series of depositions were performed to stack alternating Au (nominally 30 nm) and SiO_2 (nominally 10 nm) layers through the AuNHA mask. Besides, nominally 1 nm of Cr layer on the PET film and 1 nm of Ti layers between the alternating Au and SiO_2 layers were deposited to facilitate better adhesion. We exposed TNLNAs on the PET film by peeling off AuNHA using adhesive tape. Finally, we used 10:1 buffered oxide etchant for 10 s to open and create vertical nanogaps acting as plasmonic hotspots.[7,10,29] Figure S2 shows the FIB-SEM images of TNLNAs before and after BOE etching.

2.2. Finite-Difference Time-Domain (FDTD) Simulation. A uniform mesh size of 2 nm (x, y, and z directions) was used. The optical constants of gold were taken from Johnson and Christy. The Bloch boundary condition was used in x- and y-directions with a periodicity of 400 nm, and the perfectly matched layer boundary condition was used in the z-direction.

2.3. Optical Measurement. The extinction spectra with different RI oils were measured by a UV−vis−near-infrared (NIR) spectrophotometer. During measurements, the samples were immersed in different RI oils and covered by a 0.17 mm thick cover glass.

2.4. Raman Measurement. A confocal Raman microscope equipped with a 785 nm diode laser was used for SERS measurements. For benzenethiol (BZT) experiments, ethanol-based 1 mmol/L BZT solution was prepared, and samples were incubated overnight, followed by ethanol rinsing. Signals were recorded via 20× objective (NA = 0.4) with 1 mW laser and 1 s integration time. For different background RI, samples were covered by different RI oils with a cover glass. Typically, 100× oil immersion objective (NA = 1.25) was used with refractive index matching oil (n = 1.515) on the cover glass. Before the measurement, the instrumental calibration was verified by the silicon peak at 520 cm^{-1}. All measurements were conducted in the backscattering configuration at room temperature. Elastically scattered radiation at the wavelength corresponding to the laser line (Rayleigh scattering) was filtered out by a long-pass filter, while the rest of the collected light was guided through a multimode fiber (100 μm core diameter), acting as the pinhole for a confocal microscope, to a spectrometer. The backscatter photons were dispersed with a 300 groove/mm (750 nm blaze grating) and detected by a charge-coupled device (CCD) camera, which was thermoelectrically cooled and maintained at −60 °C. In glucose detection experiments, the sample was incubated with ethanol-based 1 mmol/L pentanethiol (PT) solution overnight, followed by ethanol rinsing. Typically, 1 mmol/L glucose solution was prepared using the phosphate-buffered saline (PBS) solution. The sample was alternately incubated with the glucose solution and washed five times with the PBS solution. Each incubation time was 10 min. Signals from a single spot were recorded via 20× objective (NA = 0.4) with 1 mW laser and 60 s integration time.

2.5. SERS EF Calculation. SERS EFs were calculated by comparing the intensities from the SERS and Raman experiments normalized by the total number of molecules contributing to the signals.[30] An equation EF = $(I_{SERS}/I_{Raman}) \times (N_{Raman}/N_{SERS})$ was used, where I_{SERS}, I_{Raman}, N_{SERS}, and N_{Raman} are the measured SERS intensity, the neat-BZT Raman intensity, and the number of BZT molecules contributing to SERS and neat Raman intensities, respectively. For I_{Raman}, we used the Raman peak at 1094 cm^{-1} originated from in-plane C−C−C ring breathing mode with the C−S stretching mode of BZT molecules. For I_{SERS}, the associated Raman peak of BZT molecules shifted to 1071 cm^{-1} due to their adsorption on the metallic surface. N_{SERS} was calculated using the equation $N_{SERS} = SA \times \rho_{SERS}$, where SA is a surface area of the SERS substrates under the focused illumination and ρ_{SERS} is the packing density of BZT on the Au surface (6.8×10^{14} molecules/cm^2).[31] N_{Raman} was calculated with the equation $N_{Raman} = A \times d_{eff} \times \rho_{Raman}$, where A is the area of focused illumination, d_{eff} is an effective focus depth of the laser beam spot, and ρ_{Raman} is the density of BZT molecules in the neat solution (5.9×10^{21} molecules/cm^3). d_{eff} was measured using a bare silicon wafer by changing the distance between the wafer and the objective lens with increments, and Raman intensity of a silicon peak (527 cm^{-1}) was used.[30]

2.6. Agar Gel Skin Phantom. To prepare an agar gel skin phantom, we used 3% agar powder dissolved in the PBS solution. The

https://dx.doi.org/10.1021/acsanm.1c00389
ACS Appl. Nano Mater. 2021, 4, 3175−3184

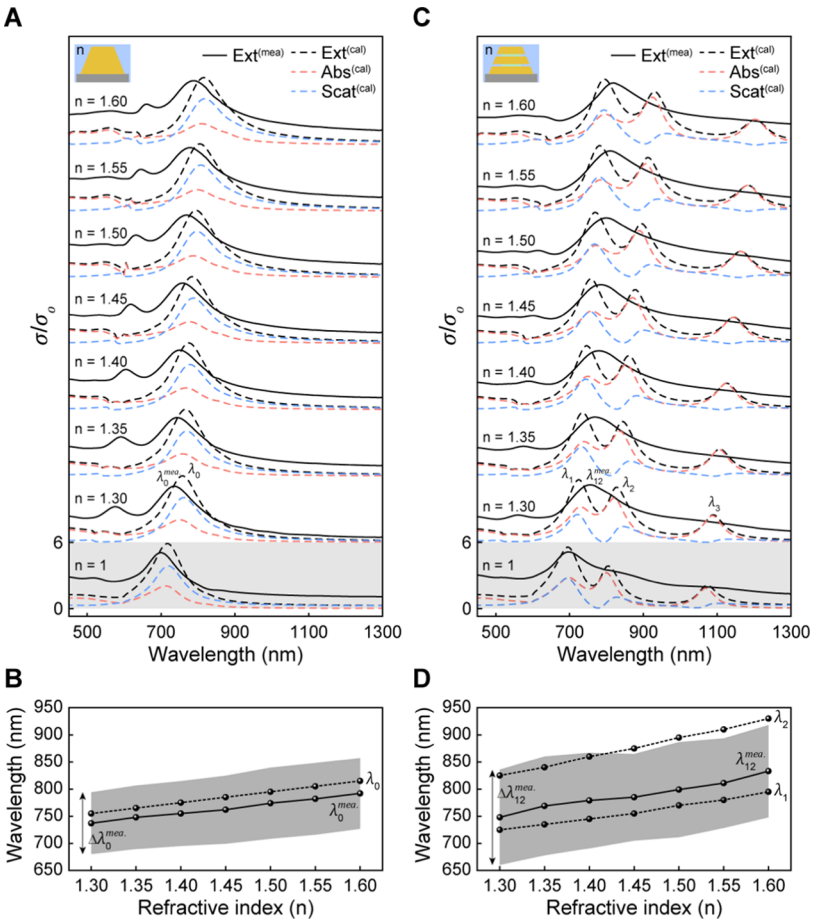

Figure 2. Far-field optical properties of TAuNPs and TNLNAs at different background RIs. Measured and FDTD-calculated extinction spectra of (A) TAuNPs and (C) TNLNAs with absorption and scattering contributions at background RI of 1 and from 1.30 to 1.60 with 0.05 increments. The spectra are offset in the *y*-axis for clarity. The RI dependence of plasmonic modes' resonant wavelengths and the measured peak line widths for (B) TAuNPs and (D) TNLNAs.

solution was boiled in a microwave and was cooled down at room temperature until complete solidification.

3. RESULTS AND DISCUSSION

3.1. Fabrication of TNLNAs. In Figure 1B,C, photograph images show good optical transparency of TNLNA arrays on polyester (PET) films. The vivid light diffraction patterns in Figure 1C reflect a uniform distribution of periodic arrays of TNLNAs. Fabrication steps are shown in Scheme 1 and the Section 2. Briefly, TNLNAs arrays were fabricated on optically transparent PET films using gold nanohole arrays (AuNHA) (periodicity = 400 nm, diameter = 180 nm, thickness = 160 nm) as a deposition mask.[25] We created TNLNAs by depositing alternating layers of Au (30 nm) and SiO_2 (10 nm) on the PET film through the AuNHA mask. The thicknesses of metal and dielectric layers were determined to achieve multiple resonances from red to near-infrared range based on our previous study that the resonant wavelengths of nanolocalized modes are tunable by controlling the thickness of dielectric layers.[23] Finally, to open the embedded plasmonic nanogap hotspots, we partially etched SiO_2 layers using buffered oxide etchant (BOE) 10:1.[7,10,29] Using the same fabrication processes, we fabricated periodic arrays of tapered-shape Au nanoparticles (TAuNPs) to serve as a reference (Figure S3). Generation of TNLNAs by electron-beam deposition of materials through the AuNHA mask provides several advantages: (i) wafer-scale, high-throughput, and reproducible fabrication; (ii) accurate nanoscale control of out-of-plane geometries to engineer plasmonic resonance properties; and (iii) facile integration of functional materials in dielectric gap layers with high optical field intensity.

3.2. Far-/Near-Field Optical Characterization. Figure 1D shows the measured extinction spectra of TAuNPs (top) and TNLNAs (bottom). As expected, TAuNPs exhibit a single-resonant feature at ≈715 nm (λ_0) originating from the ED LSP mode (Figure 1D top). In contrast, TNLNAs show two new broad resonant features at ≈850 nm (λ_2) and ≈1075 nm (λ_3) (Figure 1D bottom) in addition to a peak at ≈700 nm (λ_1). Compared to the measurement results, finite-difference time-domain (FDTD) calculations show similar extinction spectra of TAuNPs and TNLNAs with matched resonant wavelengths but much narrower line widths. Such discrepancy in resonant line widths between measurements and calculations is because the actual samples suffer from (i) the inhomogeneous broadening effect from geometrical variations between unit cells and (ii) the homogeneous broadening effect from additional optical losses due to metal−dielectric interface roughness and nanocrystalline boundaries in the metal layers. We further decomposed the total extinction loss into radiative and nonradiative decay pathways to reveal the nature of different modes by calculating scattering and absorption spectra. Notably, despite similar extinction cross-section values

https://dx.doi.org/10.1021/acsanm.1c00389
ACS Appl. Nano Mater. 2021, 4, 3175−3184

between the λ_0 mode in TAuNPs and λ_1 mode in TNLNAs, the λ_1 mode exhibits a much higher absorption-to-scattering ratio (1:1) than that of the λ_0 mode (1:2), reflecting their fundamentally different microscopic origins. Besides, we can find that the nonradiative decay processes dominate the losses for the lower-energy λ_2 and λ_3 modes in TNLNAs.

To understand the microscopic physics behind the observed far-field spectral features of TAuNPs and TNLNAs, we calculated near-field optical properties of the electric and magnetic field intensities, $|E|^2$ and $|H|^2$, and the phase of electric and magnetic fields, $\phi(E_x)$ and $\phi(H_y)$, at peak wavelengths for the different modes (Figure 1E−H). As shown in Figure 1E, the near-field mode profiles of the λ_0 peak for TAuNPs reveal an ED characteristic with a uniform $\phi(E_x)$ within the Au nanoparticle. The highly concentrated optical fields at the bottom interface between the Au nanoparticle and the dielectric substrate manifest the tapered-shape asymmetric effects on the near-field optical characteristics.[20,21] For TNLNAs, the λ_1 mode exhibits (i) ED characteristics with an in-phase $\phi(E_x)$ distribution in three Au nanodisks and (ii) MD characteristics with high magnetic fields and in-phase $\phi(H_y)$ in two MIM nanogaps (Figure 1F).[23,32] Then, the λ_2 mode reveals (i) MD characteristics with nearly in-phase $\phi(H_y)$ in the two MIM nanogaps but with a much higher magnetic field in the top MIM nanogap and (ii) electric quadrupole (EQ) characteristics with out-of-phase $\phi(E_x)$ distributions between the top and the bottom Au nanodisks (Figure 1G). Finally, the λ_3 mode displays (i) magnetic quadrupole (MQ) characteristics with nearly out-of-phase $\phi(H_y)$ in the two MIM nanogaps but with a much higher magnetic field in the bottom MIM nanogap and (ii) electric high-order multipolar characteristics with out-of-phase $\phi(E_x)$ distributions, respectively, among the top, the middle, and the bottom Au nanodisks (Figure 1H).

3.3. Plasmon Hybridization Energy Diagram. From the FDTD-calculated near-field characteristics (Figure 1F−H), we can depict a plasmon hybridization energy diagram to provide the microscopic origins of the λ_1, λ_2, and λ_3 modes in TNLNAs (Figure 1I). The red arrows and the blue loops represent the microscopic resonant sources with ED and MD characteristics and their relative phase relations. While symmetric MIM building blocks support pure ED and MD modes,[20,21,23,32] tapered-shape MIM nanostructures show bianisotropic response and support ME modes due to their coupled electric and magnetic polarizabilities.[22,33] The two elementary ME modes in the tapered-shape one-gap MIM building block, namely, ME_1 (top-gap only, Figure S4) and ME_2 (bottom-gap only, Figure S5) modes, can hybridize in the tapered-shape two-gap MIMIM nanostructure by forming a higher-energy antibonding MD electric mode (MDE_H) with MD characteristics and a lower-energy bonding MQ electric mode (MQE_L) (λ_3) with MQ characteristics. Because of its ME response with mutually coupled electric and magnetic polarizabilities, the MDE_H mode in TNLNAs is nonorthogonal to the ED mode concentrated mainly in the bottom Au nanodisk. Therefore, the MDE_H and ED modes with spatial and spectral overlaps can further hybridize by forming a higher-energy antibonding MDE_H-ED mode (λ_1) with ED and MD characteristics and a lower-energy bonding MDE_H-EQ mode (λ_2) with EQ and MD characteristics. Notably, the formation of hybridized MDE_H-ED and MDE_H-EQ modes cannot occur in symmetric MIMIM plasmonic nanostructures due to the orthogonality between modes with pure ED and MD characteristics. Therefore, while TNLNAs have the same footprint/volume compared to TAuNPs, TNLNAs can support multiple hybrid plasmonic modes with spatial overlaps and concentrated optical fields in nanogap hotspots over a wide wavelength range.

3.4. Optical Response at Different Background RIs. To investigate the RI-dependent optical responses of TAuNPs and TNLNAs, we measured and calculated extinction spectra with different background RI (n) varying from 1.30 to 1.60 (Figure 2). As shown in Figure 2A, the measured extinction spectrum of TAuNPs at n = 1.30 exhibits two resonant peaks at 580 and 741 nm (λ_0^{mea}). The peak at 580 nm originates from the Rayleigh anomaly due to the (±1,0) grating diffraction order. As the RI gradually increases from 1.30 to 1.60, the measured ED mode (λ_0^{mea}) continuously red-shifts from 741 to 792 nm. The FDTD-calculated results reveal a similar trend that the ED mode (λ_0) continuously red-shifts from 755 to 815 nm as the RI is increased from 1.30 to 1.60. Figure 2B shows the calculated and measured resonant wavelength (λ_0 and λ_0^{mea}) and the measured resonance line widths ($\Delta\lambda_0^{mea}$) for the ED mode in TAuNPs as a function of background RI. The line widths ($\Delta\lambda_0^{mea}$) of the measured ED peaks were extracted by Lorentzian fitting (Figure S6) and shown as gray shaded regions. For example, for n = 1.30 case, the line width is 114.05 ± 2.30 nm, where the uncertainty is the standard error of the average. The uncertainties of the line widths at different background RIs for both TAuNPs and TNLNAs are summarized in Table S1. The measured peak (λ_0^{mea}) reveals a RI-sensitivity of 183 nm per refractive index unit (RIU), in good agreement with the FDTD-calculated RI-sensitivity as 200 nm/RIU for the ED mode (λ_0).

For TNLNAs at n = 1.30, the measured extinction spectrum exhibits a broader resonant feature (λ_{12}^{mea}) at 756 nm with a line width of 175.77 ± 3.66 nm resulting from spectral overlaps of the λ_1 and λ_2 modes (Figure 2C). Unlike the measured extinction spectrum of TNLNAs in the air (n = 1), the extinction spectra of TNLNAs immersed in RI oils do not reveal apparent shoulder features associated with the λ_2 and λ_3 modes. This observation is likely because the spatially nonuniform parallelism between the TNLNA plane and the two cover glass surfaces can disrupt and blur the incident light directionality by inducing additional inhomogeneous broadening of spectral extinction features. As the RI increases from 1.30 to 1.60, the measured peak (λ_{12}^{mea}) red-shifts gradually from 756 to 819 nm with spectral line widths slightly varying between 159.74 ± 3.17 nm (minimum at n = 1.45) and 182.36 ± 4.00 nm (maximum at n = 1.35). The FDTD calculations show three distinct modes at 725 nm (λ_1), 825 nm (λ_2), and 1090 nm (λ_3). With the background RI increased from 1.30 to 1.60, the λ_1, λ_2, and λ_3 modes red-shift from 725 to 795 nm, from 825 to 930 nm, and from 1090 to 1205 nm, respectively. The measured broad feature λ_{12}^{mea} reflects the average optical response of the spectrally overlapped λ_1 and λ_2 modes in response to the RI changes. Furthermore, the FDTD calculations reveal that the three modes in TNLNAs can maintain higher absorption cross-sections at different background RIs than that of the ED mode in TAuNPs.

Figure 2D highlights several critical observations in the RI-dependent optical properties of TNLNAs. First, the λ_2 and λ_3 modes possess higher calculated RI-sensitivities of 350 and 383 nm/RIU than that of 233 nm/RIU for the λ_1 mode because the λ_2 and λ_3 modes exhibit higher optical energy concentration in MIM nanogaps with a higher susceptibility to the background RI changes (Figure 1G,H). Second, due to

https://dx.doi.org/10.1021/acsanm.1c00389
ACS Appl. Nano Mater. 2021, 4, 3175−3184

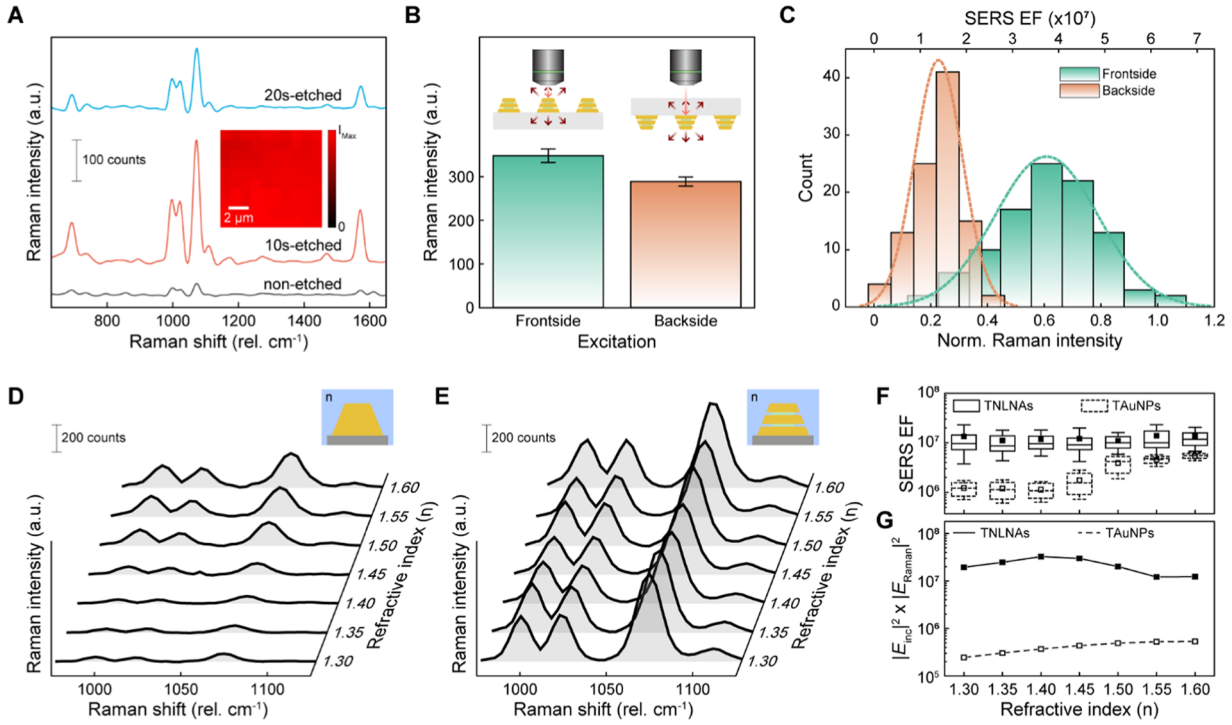

Figure 3. Backside-excitable TNLNAs show uniform hotspot arrays with high sensitivity and RI-insensitivity. (A) Measured average SERS spectra of BZT for TNLNAs with different etching times, inset: a 2D Raman image using a BZT Raman peak of 1071 cm^{-1}. The spectra are offset in the *y*-axis for clarity. (B) SERS intensities measured from frontside and backside. The error bars show 1 standard deviation from 100 pixels. (C) Histograms of SERS intensities and corresponding SERS EFs for frontside and backside configurations. The measured average SERS spectra of BZT at different background RI for (D) TAuNPs and (E) TNLNAs. (F) Measured SERS EFs of TAuNPs and TNLNAs at different background RI. The error bars show 1 standard deviation from 100 pixels. The bars in boxes from bottom to top are 25th quartile, median, and 75th quartile values from 100 pixels. The square represents the mean value. (G) Calculated maximum electric field enhancement using the laser excitation (785 nm) and Stokes-shifted (860 nm) wavelengths for TAuNPs (dashed) and TNLNAs (solid).

its hybrid ED and MD nature (Figure 1F), the λ_1 mode in TNLNAs exhibits a slightly larger RI-sensitivity of 233 nm/RIU than that of 200 nm/RIU for the λ_0 mode with a pure ED nature in TAuNPs. Finally, the average RI-sensitivity for the λ_1 and λ_2 modes is 291 nm/RIU, agreeing with 283 nm/RIU for the measured λ_{12}^{mea} feature. Besides, the line width $\Delta\lambda_{12}^{mea}$ matches with the overlapped spectral range for the λ_1 and λ_2 modes. Therefore, compared to TAuNPs of the same nanoscale footprint and volume, TNLNAs have a broader multiresonant response with higher absorption upon large background RI variations from 1.30 to 1.60.

3.5. SERS Characterization and Performance at Different Background RIs. To evaluate the SERS performance, we measured SERS spectra of TNLNAs coated with a self-assembled monolayer (SAM) of benzenethiol (BZT) molecules. Notably, BZT is a nonresonant Raman probe molecule under 785 nm laser excitation. We first assessed the dependence of the TNLNAs' SERS performance on the wet-etching process. After the BOE-based wet-etching, the embedded plasmonic nanogap hotspots within SiO_2 layers in TNLNAs can be exposed to analyte molecules in the environment.[7,10,34] We performed two-dimensional (2D) Raman mapping over 10 μm × 10 μm area containing 100 pixels, and Figure 3A shows the averaged Raman spectra for TNLNAs under different etching conditions. The TNLNAs with 10 s etching reveal ≈10 times stronger Raman intensity than the nonetched case at 1071 cm^{-1} since molecules can access the previously embedded hotspots. More specifically, the 10 s etched sample's SERS intensities are 348.23 ± 15.43 CCD counts, and the SERS intensities of the nonetched sample are 34.46 ± 4.48 CCD counts. The uncertainties are 1 standard deviation obtained from 100 individual pixels. The inset 2D Raman image supports the excellent uniformity of TNLNAs with a relative standard deviation (RSD) value of 4.4%, where RSD is the ratio of the standard deviation to the mean. As the etching time increases from 10 to 20 s, the signal intensity decreases (143.79 ± 26.32 CCD counts), which is still ≈4.2 times higher than the nonetched one. The significantly increased RSD value from 4.4 to 18.3% indicates the geometrical deformation of plasmonic nanogap hotspots in TNLNAs due to the overetching of SiO_2 layers (Figure S7). To examine the backside excitability of TNLNAs on the transparent PET film, we performed SERS measurements by probing BZT signals from both frontside and backside, as shown in Figure 3B (full SERS spectra shown in Figure S8). SERS measurements through backside excitation reveal an outstanding uniformity (RSD = 3.6%) and a similar SERS intensity (86%) compared to the frontside excitation. Furthermore, TNLNAs-based SERS substrates exhibit improved SERS performance than the reported backside-excitable SERS substrates, which suffer from significantly dropped signal intensities by 0.5 or 0.7 fold by switching from the frontside to backside excitation condition.[35,36]

Figure 3C illustrates the histograms of 1071 cm^{-1} Raman signal intensities and corresponding SERS EFs from 100 pixels on TNLNAs under frontside and backside excitation conditions (see the Section 2 for the details in SERS EF calculation).[30] The histograms of SERS signals under frontside

https://dx.doi.org/10.1021/acsanm.1c00389
ACS Appl. Nano Mater. 2021, 4, 3175−3184

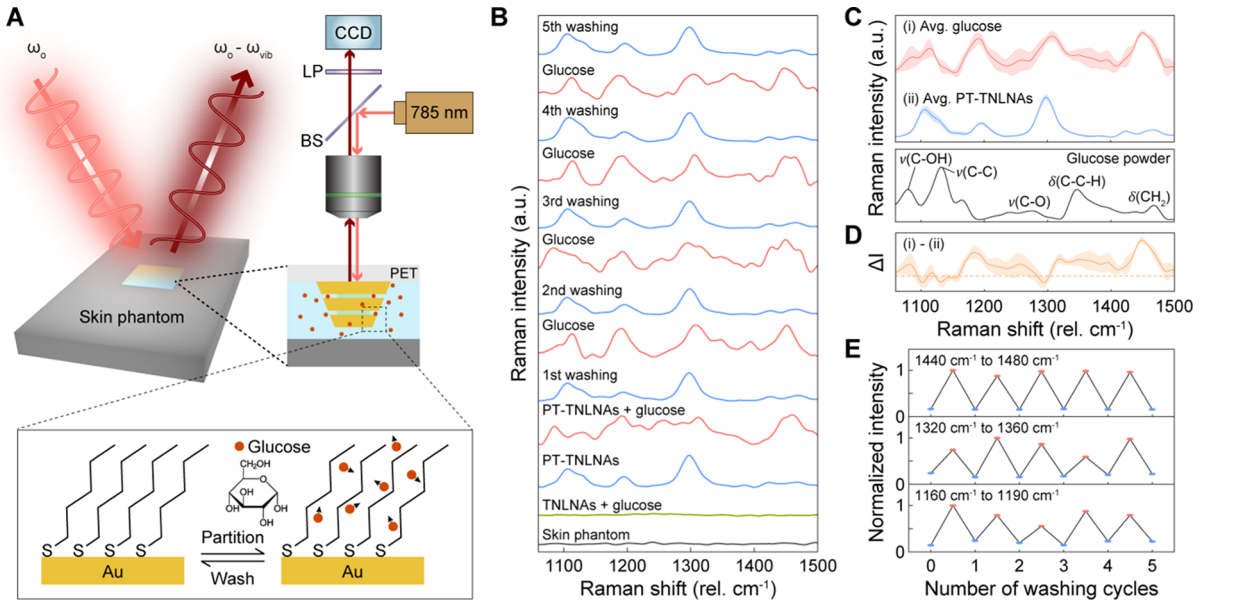

Figure 4. In situ SERS detection of glucose on a skin phantom by TNLNAs. (A) Schematic illustration of the experimental setup. CCD, charge-coupled device; LP, long-pass filter; and BS, beam splitter; (B) measured SERS spectra for glucose sensing with five washing cycles. The spectra are offset in the *y*-axis for clarity. (C) Averaged SERS spectra with and without glucose (top) and Raman spectrum of glucose powder under high laser power (20 mW) (bottom). Note: ν = stretching mode and δ = bending mode. (D) SERS spectrum obtained by subtracting (ii) from (i) in (C). (E) Normalized glucose SERS intensities with three different regions over five washing cycles.

and backside excitations fit the normal distribution function, revealing an excellent uniformity. The average SERS EFs under frontside and backside excitations are 3.7×10^7 and 1.4×10^7, respectively, high enough for single-molecule level detection.[8,30] Then, we compared RI-dependent SERS performances between TAuNPs and TNLNAs, as shown in Figure 3D,E. TAuNPs reveal a RI-sensitive SERS response with gradually increased SERS intensities as the background RI increases from 1.30 to 1.60. This trend agrees with the measurement and calculation results for the RI-dependent extinction spectra of TAuNPs (Figure 2A), showing that the RI increase can gradually red-shift the ED mode from off-resonant to on-resonant conditions in SERS measurements under 785 nm laser excitation. On the contrary, TNLNAs show more stable SERS signal intensities in response to background RI variations between 1.30 and 1.60. In Figure 3F, we plotted the SERS EFs from measurements as a function of RI. Notably, TNLNAs show consistently high SERS EFs ($>10^7$) insensitive to RI changes between 1.30 and 1.60, whereas the SERS EFs of TAuNPs vary by 1 order of magnitude in the same RI range. The microscopic origin of TNLNAs' RI-insensitive high SERS EFs is due to their broadband plasmonic response by supporting multiple hybridized LSP modes with highly concentrated optical fields in nanogap hotspots over a wide spectral range, covering the excitation laser wavelength under different background RIs.

In Figure 3G, we conducted simulation studies to corroborate the experimental observation. The estimated $|E|^4$ values, as $|E_{inc}|^2 \times |E_{Raman}|^2$, were calculated using the excitation (785 nm) and Stokes-shifted wavelengths (860 nm, i.e., 1071 cm^{-1}) as a function of background RI. For TNLNAs, the calculated $|E_{inc}|^2 \times |E_{Raman}|^2$ values vary between 1.2×10^7 and 3.3×10^7 with the same order of magnitude compared to the measured SERS EFs in the RI range between 1.30 and 1.60. In contrast, for TAuNPs, the calculated $|E_{inc}|^2 \times |E_{Raman}|^2$ values monotonically increase from 2.4×10^5 to 5.4×10^5 as the background RI increases from 1.30 and 1.60 and show nearly 1 order of magnitude difference compared to the measured SERS EFs. The measured SERS EFs result from the surface-modified BZT molecule ensembles distributed over multiple hotspots within a diffraction-limited excitation laser spot (diameter of ≈300 nm). FDTD-calculated values are from a single hotspot. The relatively larger discrepancy between the calculated values and measured SERS EFs for TAuNPs is likely because FDTD calculations did not consider the local field enhancements from the surface roughness effects. Therefore, the unique properties of vertical multi-nanogap-based TNLNAs, including (i) RI-insensitivity with high SERS EF ($>10^7$), (ii) excellent uniformity with high-throughput and scalable fabrication, (iii) optical transparency allowing backside excitation, and (iv) mechanical flexibility, can potentially enable spatiotemporally resolved biochemical analysis with TNLNAs as wearable SERS biochemical sensors for point-of-care diagnostics and as patchlike chemical sensors to perform in situ SERS analysis for samples in which extraction of molecules is impossible or difficult.

3.6. In Situ SERS Detection of Glucose on a Skin Phantom. To demonstrate TNLNAs' capability for in situ SERS measurements, we exploited transparent flexible TNLNAs for label-free monitoring of glucose molecules on the skin phantom. As shown in Figure 4A, during the SERS measurements under the backside excitation, the TNLNAs' SERS substrate was placed to interface with an agar gel layer and glucose molecules (1 mmol/L). Here, the agar gel serves as a transparent skin phantom to contain solution fluids with analyte molecules,[37,38] and the phosphate-buffered-saline (PBS)-based glucose solutions can mimic the sweat fluid in correlation with blood glucose level.[39] Before the measurements, to mitigate the very weak binding of glucose to the metal surface, TNLNAs were incubated in 1 mmol/L pentanethiol (PT) to form a uniform SAM as a partition layer to enrich glucose at plasmonic hotspots in SERS

https://dx.doi.org/10.1021/acsanm.1c00389
ACS Appl. Nano Mater. 2021, 4, 3175−3184

monitoring (Figure 4A). Hydrophobic interactions between the glucose molecules and straight chains of alkanethiol SAM can increase glucose dwell time at hotspot regions.[40−42] To test the reversible and reusable detection capability, we exposed the PT-functionalized TNLNAs in glucose solution, performed SERS measurements, washed the SERS substrates, and repeated these processes five times (Figure 4B). The agar gel skin phantom, as the control sample, did not show any distinct Raman peaks (gray). Without the PT partition layer modification (green), no glucose Raman peaks can be observed for TNLNAs in agreement with the previous study.[40] Over the five glucose incubation (red) and PBS washing (blue) cycles, we observed repetitive changes of SERS profiles in the regions related to glucose Raman features at ≈1080 cm^{-1} of ν(C−OH), ≈1122 cm^{-1} of ν(C−C), ≈1255 cm^{-1} of ν(C−O), ≈1340 cm^{-1} of δ(C−C−H), and ≈1460 cm^{-1} of $\delta(CH_2)$,[43] where ν denotes the stretching mode and δ denotes the bending mode. After each washing cycle, the measured SERS spectra show reproducible Raman features associated with the PT layer coated on TNLNAs. Nevertheless, the Raman features related to glucose show inconsistent spectral profiles between five different cycles with a significant standard deviation, shown in Figure 4C (top). The significant variations in glucose-related Raman profiles reflect the stochastic trapping of glucose molecules in the PT partition layer, which can cause varying position-orientation configurations of glucose ensembles at plasmonic hotspots.[12,40,41,44] Figure 4D shows the subtracted SERS spectrum between the averaged SERS spectra of glucose incubation and PBS washing cycles, which can be compared with the Raman spectrum of glucose powder (Figure 4C, bottom). Interestingly, the trapping of glucose molecules in the PT partition layer can induce larger and much more consistent Raman intensity changes in the spectral region of the $\delta(CH_2)$ mode at ≈1460 cm^{-1} than other glucose modes. This observation manifests that the hydrophobic interactions between glucose and PT can reduce the glucose rotational degree of freedom and specifically increase the alignment of the $\delta(CH_2)$ mode transition dipole moment with plasmonic optical fields at hotspots. To better show the reversibility of glucose detection on the skin phantom, we plotted the normalized intensities of three glucose relevant ranges, including 1440−1480, 1320−1360, and 1160−1190 cm^{-1} between different washing and incubation cycles in Figure 4E. Compared to the spectral region of the $\delta(CH_2)$ mode (1440−1480 cm^{-1}), the other two regions of the δ(C−C−H) mode (1320−1360 cm^{-1}) and the ν(C−C) mode (1160−1190 cm^{-1}) of glucose in the PT layer show reduced consistency due to more considerable orientation variations of transition dipole moments for these two modes. The label-SERS approach based on Raman tags (or reporters) such as mercaptophenyl boronic acid can improve glucose SERS detection and analysis with reduced spectral variations between different measurement cycles.

4. CONCLUSIONS

In summary, we have demonstrated that TNLNAs consisting of vertically stacked MIM nanodisks can enable RI-insensitive high SERS EFs under both frontside and backside laser excitation conditions. From the theoretical analysis and numerical simulations, we reveal that TNLNAs can support multiple hybridized LSP modes to achieve a broadband multiresonant optical concentration at hotspots for good spectral matching with the excitation laser wavelength under widely varying background RIs. By integrating uniform arrays of TNLNAs with PT modifications on flexible transparent PET substrates, we have conducted the backside-excitable SERS measurements of glucose molecules on a skin phantom to demonstrate the potential utility for rapid in situ biomedical diagnostics. Notably, the nanoscale footprint and volume of individual TNLNAs can allow their integration with other types of nanodevices to achieve nanoscale multifunctionality. Therefore, RI-insensitive high-performance TNLNAs with optical transparency can be a promising wearable SERS platform for real-time biochemical sensing in a spatiotemporally resolved manner.

■ ASSOCIATED CONTENT

Supporting Information

The Supporting Information is available free of charge at https://pubs.acs.org/doi/10.1021/acsanm.1c00389.

FIB-SEM images of TNLNAs before and after wet etching; FIB-SEM image of TAuNPs; FDTD-calculated extinction spectra of top-gap and bottom-gap only TNLNAs with distribution maps of $|E|^2$, $|H|^2$, $\phi(H_y)$, and $\phi(E_x)$ at resonant wavelengths; Lorentzian fitting to extract the line widths of the resonance peaks for TNLNAs; 2D BZT Raman images of different etching conditions; average BZT SERS spectra using frontside and backside excitation; and table of extracted line widths for TAuNPs and TNLNAs with different background RIs (PDF)

■ AUTHOR INFORMATION

Corresponding Author

Wei Zhou − *Department of Electrical and Computer Engineering, Virginia Tech, Blacksburg, Virginia 24061, United States;* orcid.org/0000-0002-5257-3885; Email: wzh@vt.edu

Authors

Wonil Nam − *Department of Electrical and Computer Engineering, Virginia Tech, Blacksburg, Virginia 24061, United States;* orcid.org/0000-0002-7804-3049

Junyeob Song − *Physical Measurement Laboratory, National Institute of Standards and Technology, Gaithersburg, Maryland 20899, United States*

Seied Ali Safiabadi Tali − *Department of Electrical and Computer Engineering, Virginia Tech, Blacksburg, Virginia 24061, United States*

Henri J. Lezec − *Physical Measurement Laboratory, National Institute of Standards and Technology, Gaithersburg, Maryland 20899, United States*

Amit Agrawal − *Physical Measurement Laboratory, National Institute of Standards and Technology, Gaithersburg, Maryland 20899, United States; Institute for Research in Electronics and Applied Physics and Maryland NanoCenter, University of Maryland, College Park, Maryland 20742, United States;* orcid.org/0000-0002-9619-7623

Complete contact information is available at: https://pubs.acs.org/10.1021/acsanm.1c00389

Notes

The authors declare no competing financial interest.

https://dx.doi.org/10.1021/acsanm.1c00389
ACS Appl. Nano Mater. 2021, 4, 3175−3184

■ ACKNOWLEDGMENTS

The authors gratefully acknowledge funding support from the Air Force Office of Scientific Research (AFOSR) Young Investigator Award FA9550-18-1-0328 and National Institute of Standards and Technology (NIST) grants 70NANB18H201 and 70NANB19H163. A.A. and W.Z. acknowledge support under the Cooperative Research Agreement between the University of Maryland and the National Institute of Standards and Technology Physical Measurement Laboratory, Award 70NANB14H209, through the University of Maryland.

■ REFERENCES

(1) Langer, J.; Jimenez de Aberasturi, D.; Aizpurua, J.; Alvarez-Puebla, R. A.; Auguie, B.; Baumberg, J. J.; Bazan, G. C.; Bell, S. E. J.; Boisen, A.; Brolo, A. G.; Choo, J.; Cialla-May, D.; Deckert, V.; Fabris, L.; Faulds, K.; Garcia de Abajo, F. J.; Goodacre, R.; Graham, D.; Haes, A. J.; Haynes, C. L.; Huck, C.; Itoh, T.; Kall, M.; Kneipp, J.; Kotov, N. A.; Kuang, H.; Le Ru, E. C.; Lee, H. K.; Li, J. F.; Ling, X. Y.; Maier, S. A.; Mayerhofer, T.; Moskovits, M.; Murakoshi, K.; Nam, J. M.; Nie, S.; Ozaki, Y.; Pastoriza-Santos, I.; Perez-Juste, J.; Popp, J.; Pucci, A.; Reich, S.; Ren, B.; Schatz, G. C.; Shegai, T.; Schlucker, S.; Tay, L. L.; Thomas, K. G.; Tian, Z. Q.; Van Duyne, R. P.; Vo-Dinh, T.; Wang, Y.; Willets, K. A.; Xu, C.; Xu, H.; Xu, Y.; Yamamoto, Y. S.; Zhao, B.; Liz-Marzan, L. M. Present and Future of Surface-Enhanced Raman Scattering. *ACS Nano* **2020**, *14*, 28−117.

(2) Ding, S.-Y.; Yi, J.; Li, J.-F.; Ren, B.; Wu, D.-Y.; Panneerselvam, R.; Tian, Z.-Q. Nanostructure-based plasmon-enhanced Raman spectroscopy for surface analysis of materials. *Nat. Rev. Mater.* **2016**, *1*, No. 16021.

(3) Brolo, A. G. Plasmonics for future biosensors. *Nat. Photonics* **2012**, *6*, 709−713.

(4) Rodrigo, D.; Limaj, O.; Janner, D.; Etezadi, D.; de Abajo, F. J. G.; Pruneri, V.; Altug, H. Mid-infrared plasmonic biosensing with graphene. *Science* **2015**, *349*, 165−168.

(5) Liu, P. Y.; Chin, L. K.; Ser, W.; Chen, H. F.; Hsieh, C. M.; Lee, C. H.; Sung, K. B.; Ayi, T. C.; Yap, P. H.; Liedberg, B.; Wang, K.; Bourouina, T.; Leprince-Wang, Y. Cell refractive index for cell biology and disease diagnosis: past, present and future. *Lab Chip* **2016**, *16*, 634−644.

(6) Chatterjee, A.; Cerna Sanchez, J. A.; Yamauchi, T.; Taupin, V.; Couvrette, J.; Gorodetsky, A. A. Cephalopod-inspired optical engineering of human cells. *Nat. Commun.* **2020**, *11*, No. 2708.

(7) Nam, W.; Ren, X.; Tali, S. A. S.; Ghassemi, P.; Kim, I.; Agah, M.; Zhou, W. Refractive-Index-Insensitive Nanolaminated SERS Substrates for Label-Free Raman Profiling and Classification of Living Cancer Cells. *Nano Lett.* **2019**, *19*, 7273−7281.

(8) Lim, D. K.; Jeon, K. S.; Hwang, J. H.; Kim, H.; Kwon, S.; Suh, Y. D.; Nam, J. M. Highly uniform and reproducible surface-enhanced Raman scattering from DNA-tailorable nanoparticles with 1-nm interior gap. *Nat. Nanotechnol.* **2011**, *6*, 452−460.

(9) Jeong, J. W.; Arnob, M. M.; Baek, K. M.; Lee, S. Y.; Shih, W. C.; Jung, Y. S. 3D Cross-Point Plasmonic Nanoarchitectures Containing Dense and Regular Hot Spots for Surface-Enhanced Raman Spectroscopy Analysis. *Adv. Mater.* **2016**, *28*, 8695−8704.

(10) Song, J.; Nam, W.; Zhou, W. Scalable High-Performance Nanolaminated SERS Substrates Based on Multistack Vertically Oriented Plasmonic Nanogaps. *Adv. Mater. Technol.* **2019**, *4*, No. 1800689.

(11) Song, J.; Cheng, W.; Nie, M.; He, X.; Nam, W.; Cheng, J.; Zhou, W. Partial Leidenfrost Evaporation-Assisted Ultrasensitive Surface-Enhanced Raman Spectroscopy in a Janus Water Droplet on Hierarchical Plasmonic Micro-/Nanostructures. *ACS Nano* **2020**, *14*, 9521−9531.

(12) Wang, X.; Huang, S.-C.; Hu, S.; Yan, S.; Ren, B. Fundamental understanding and applications of plasmon-enhanced Raman spectroscopy. *Nat. Rev. Phys.* **2020**, *2*, 253−271.

(13) Xu, K.; Zhou, R.; Takei, K.; Hong, M. Toward Flexible Surface-Enhanced Raman Scattering (SERS) Sensors for Point-of-Care Diagnostics. *Adv. Sci.* **2019**, *6*, No. 1900925.

(14) Garg, A.; Nam, W.; Zhou, W. Reusable Surface-Enhanced Raman Spectroscopy Membranes and Textiles via Template-Assisted Self-Assembly and Micro/Nanoimprinting. *ACS Appl. Mater. Interfaces* **2020**, *12*, 56290−56299.

(15) Robinson, J. T.; Jorgolli, M.; Shalek, A. K.; Yoon, M. H.; Gertner, R. S.; Park, H. Vertical nanowire electrode arrays as a scalable platform for intracellular interfacing to neuronal circuits. *Nat. Nanotechnol.* **2012**, *7*, 180−184.

(16) Xie, C.; Lin, Z.; Hanson, L.; Cui, Y.; Cui, B. Intracellular recording of action potentials by nanopillar electroporation. *Nat. Nanotechnol.* **2012**, *7*, 185−190.

(17) Xiao, S.; Drachev, V. P.; Kildishev, A. V.; Ni, X.; Chettiar, U. K.; Yuan, H. K.; Shalaev, V. M. Loss-free and active optical negative-index metamaterials. *Nature* **2010**, *466*, 735−738.

(18) Poddubny, A.; Iorsh, I.; Belov, P.; Kivshar, Y. Hyperbolic metamaterials. *Nat. Photonics* **2013**, *7*, 948−957.

(19) Sreekanth, K. V.; Alapan, Y.; ElKabbash, M.; Ilker, E.; Hinczewski, M.; Gurkan, U. A.; De Luca, A.; Strangi, G. Extreme sensitivity biosensing platform based on hyperbolic metamaterials. *Nat. Mater.* **2016**, *15*, 621−627.

(20) Dmitriev, A.; Pakizeh, T.; Kall, M.; Sutherland, D. S. Gold-silica-gold nanosandwiches: tunable bimodal plasmonic resonators. *Small* **2007**, *3*, 294−299.

(21) Frederiksen, M.; Bochenkov, V. E.; Ogaki, R.; Sutherland, D. S. Onset of bonding plasmon hybridization preceded by gap modes in dielectric splitting of metal disks. *Nano Lett.* **2013**, *13*, 6033−6039.

(22) Alaee, R.; Albooyeh, M.; Yazdi, M.; Komjani, N.; Simovski, C.; Lederer, F.; Rockstuhl, C. Magneto-electric coupling in nonidentical plasmonic nanoparticles: Theory and applications. *Phys. Rev. B: Condens. Matter Mater. Phys.* **2015**, *91*, No. 115119.

(23) Song, J.; Zhou, W. Multiresonant Composite Optical Nanoantennas by Out-of-plane Plasmonic Engineering. *Nano Lett.* **2018**, *18*, 4409−4416.

(24) Maccaferri, N.; Zhao, Y.; Isoniemi, T.; Iarossi, M.; Parracino, A.; Strangi, G.; De Angelis, F. Hyperbolic Meta-Antennas Enable Full Control of Scattering and Absorption of Light. *Nano Lett.* **2019**, *19*, 1851−1859.

(25) Henzie, J.; Lee, M. H.; Odom, T. W. Multiscale patterning of plasmonic metamaterials. *Nat. Nanotechnol.* **2007**, *2*, 549−554.

(26) Qin, D.; Xia, Y.; Whitesides, G. M. Soft lithography for micro- and nanoscale patterning. *Nat. Protoc.* **2010**, *5*, 491−502.

(27) Zhou, W.; Dridi, M.; Suh, J. Y.; Kim, C. H.; Co, D. T.; Wasielewski, M. R.; Schatz, G. C.; Odom, T. W. Lasing action in strongly coupled plasmonic nanocavity arrays. *Nat. Nanotechnol.* **2013**, *8*, 506−511.

(28) Fernandez-Bravo, A.; Wang, D.; Barnard, E. S.; Teitelboim, A.; Tajon, C.; Guan, J.; Schatz, G. C.; Cohen, B. E.; Chan, E. M.; Schuck, P. J.; Odom, T. W. Ultralow-threshold, continuous-wave upconverting lasing from subwavelength plasmons. *Nat. Mater.* **2019**, *18*, 1172−1176.

(29) Ren, X.; Nam, W.; Ghassemi, P.; Strobl, J. S.; Kim, I.; Zhou, W.; Agah, M. Scalable nanolaminated SERS multiwell cell culture assay. *Microsyst. Nanoeng.* **2020**, *6*, No. 47.

(30) Le Ru, E. C.; Blackie, E.; Meyer, M.; Etchegoin, P. G. Surface Enhanced Raman Scattering Enhancement Factors: A Comprehensive Study. *J. Phys. Chem. C* **2007**, *111*, 13794−13803.

(31) Ishida, T.; Choi, N.; Mizutani, W.; Tokumoto, H.; Kojima, I.; Azehara, H.; Hokari, H.; Akiba, U.; Fujihira, M. High-resolution X-ray photoelectron spectra of organosulfur monolayers on Au(111): S(2p) spectral dependence on molecular species. *Langmuir* **1999**, *15*, 6799−6806.

(32) Liu, N.; Fu, L.; Kaiser, S.; Schweizer, H.; Giessen, H. Plasmonic Building Blocks for Magnetic Molecules in Three-Dimensional Optical Metamaterials. *Adv. Mater.* **2008**, *20*, 3859−3865.

(33) Sonnefraud, Y.; Verellen, N.; Sobhani, H.; Vandenbosch, G. A. E.; Moshchalkov, V. V.; Van Dorpe, P.; Nordlander, P.; Maier, S. A.

https://dx.doi.org/10.1021/acsanm.1c00389
ACS Appl. Nano Mater. 2021, 4, 3175−3184

Experimental Realization of Subradiant, Superradiant, and Fano Resonances in Ring/Disk Plasmonic Nanocavities. *ACS Nano* **2010**, *4*, 1664−1670.
(34) Nam, W.; Zhao, Y.; Song, J.; Ali Safiabadi Tali, S.; Kang, S.; Zhu, W.; Lezec, H. J.; Agrawal, A.; Vikesland, P. J.; Zhou, W. Plasmonic Electronic Raman Scattering as Internal Standard for Spatial and Temporal Calibration in Quantitative Surface-Enhanced Raman Spectroscopy. *J. Phys. Chem. Lett.* **2020**, *11*, 9543−9551.
(35) Yamazoe, S.; Naya, M.; Shiota, M.; Morikawa, T.; Kubo, A.; Tani, T.; Hishiki, T.; Horiuchi, T.; Suematsu, M.; Kajimura, M. Large-area surface-enhanced Raman spectroscopy imaging of brain ischemia by gold nanoparticles grown on random nanoarrays of transparent boehmite. *ACS Nano* **2014**, *8*, 5622−5632.
(36) Wu, K.; Nguyen, L. Q.; Rindzevicius, T.; Keller, S. S.; Boisen, A. Wafer-Scale Polymer-Based Transparent Nanocorals with Excellent Nanoplasmonic Photothermal Stability for High-Power and Superfast SERS Imaging. *Adv. Opt. Mater.* **2019**, *7*, No. 1901413.
(37) Pogue, B. W.; Patterson, M. S. Review of tissue simulating phantoms for optical spectroscopy, imaging and dosimetry. *J. Biomed. Opt.* **2006**, *11*, No. 041102.
(38) Park, J. E.; Yonet-Tanyeri, N.; Vander Ende, E.; Henry, A. I.; Perez White, B. E.; Mrksich, M.; Van Duyne, R. P. Plasmonic Microneedle Arrays for in Situ Sensing with Surface-Enhanced Raman Spectroscopy (SERS). *Nano Lett.* **2019**, *19*, 6862−6868.
(39) Lee, H.; Hong, Y. J.; Baik, S.; Hyeon, T.; Kim, D. H. Enzyme-Based Glucose Sensor: From Invasive to Wearable Device. *Adv. Healthcare Mater.* **2018**, *7*, No. e1701150.
(40) Shafer-Peltier, K. E.; Haynes, C. L.; Glucksberg, M. R.; Van Duyne, R. P. Toward a glucose biosensor based on surface-enhanced Raman scattering. *J. Am. Chem. Soc.* **2003**, *125*, 588−593.
(41) Yonzon, C. R.; Haynes, C. L.; Zhang, X.; Walsh, J. T., Jr.; Van Duyne, R. P. A glucose biosensor based on surface-enhanced Raman scattering: improved partition layer, temporal stability, reversibility, and resistance to serum protein interference. *Anal. Chem.* **2004**, *76*, 78−85.
(42) Bantz, K. C.; Nelson, H. D.; Haynes, C. L. Plasmon-Enabled Study of Self-Assembled Alkanethiol Ordering on Roughened Ag Substrates. *J. Phys. Chem. C* **2012**, *116*, 3585−3593.
(43) Söderholm, S.; Roos, Y. H.; Meinander, N.; Hotokka, M. Raman spectra of fructose and glucose in the amorphous and crystalline states. *J. Raman Spectrosc.* **1999**, *30*, 1009−1018.
(44) Lindquist, N. C.; de Albuquerque, C. D. L.; Sobral-Filho, R. G.; Paci, I.; Brolo, A. G. High-speed imaging of surface-enhanced Raman scattering fluctuations from individual nanoparticles. *Nat. Nanotechnol.* **2019**, *14*, 981−987.

https://dx.doi.org/10.1021/acsanm.1c00389
ACS Appl. Nano Mater. 2021, 4, 3175−3184